Europace (2014) **16**, 133–141
doi:10.1093/europace/eut229

BASIC SCIENCE

Navigated DENSE strain imaging for post-radiofrequency ablation lesion assessment in the swine left atria

Ehud J. Schmidt[1], Maggie M. Fung[2], Pelin Aksit Ciris[3], Ting Song[4], Ajit Shankaranarayanan[4], Godtfred Holmvang[5], Sandeep N. Gupta[6], Miguel Chaput[5], Robert A. Levine[5], Jeremy Ruskin[5], Vivek Y. Reddy[7], Andre D'avila[7], Anthony H. Aletras[8], and Stephan B. Danik[5]*

[1]Department of Radiology, Brigham and Women's Hospital, Boston, MA 02115, USA; [2]GE Healthcare MR, Waukesha, WI 53051, USA; [3]Department of Biomedical Engineering, Yale University, New Haven, CT 06520, USA; [4]GE Healthcare Applied Science Lab, Bethesda, MD 20892, USA; [5]Department of Cardiology, Massachusetts General Hospital, 55 Fruit Street, GRB109, Boston, MA 02104, USA; [6]GE Global Research, Niskayuna, NY 12309, USA; [7]Department of Cardiology, Mt. Sinai Medical School, New York, NY 10029, USA; and [8]Department of Biomedical Informatics, University Central Greece, Lamia 35100, Greece

Received 19 March 2013; accepted after revision 28 June 2013; online publish-ahead-of-print 6 September 2013

Aims Prior work has demonstrated that magnetic resonance imaging (MRI) strain can separate necrotic/stunned myocardium from healthy myocardium in the left ventricle (LV). We surmised that high-resolution MRI strain, using navigator-echo-triggered DENSE, could differentiate radiofrequency ablated tissue around the pulmonary vein (PV) from tissue that had not been damaged by radiofrequency energy, similarly to navigated 3D myocardial delayed enhancement (3D-MDE).

Methods and results A respiratory-navigated 2D-DENSE sequence was developed, providing strain encoding in two spatial directions with $1.2 \times 1.0 \times 4\ mm^3$ resolution. It was tested in the LV of infarcted sheep. In four swine, incomplete circumferential lesions were created around the right superior pulmonary vein (RSPV) using ablation catheters, recorded with electro-anatomic mapping, and imaged 1 h later using atrial-diastolic DENSE and 3D-MDE at the left atrium/RSPV junction. DENSE detected ablation gaps (regions with $>12\%$ strain) in similar positions to 3D-MDE (2D cross-correlation 0.89 ± 0.05). Low-strain ($<8\%$) areas were, on average, 33% larger than equivalent MDE regions, so they include both injured and necrotic regions. Optimal DENSE orientation was perpendicular to the PV trunk, with high shear strain in adjacent viable tissue appearing as a sensitive marker of ablation lesions.

Conclusions Magnetic resonance imaging strain may be a non-contrast alternative to 3D-MDE in intra-procedural monitoring of atrial ablation lesions.

Keywords Magnetic resonance imaging ablation • Atrial fibrillation • Porcine model

Introduction

In patients with paroxysmal atrial fibrillation (AF), electrical isolation is typically achieved at the time of the radiofrequency ablation (RFA) procedure,[1,2] but reconnection of the pulmonary vein (PV) to the atrium is frequently the cause of clinical recurrences.[3,4] It is suspected that reconnection occurs due to gaps in the lesion set as well as at sites of insufficient ablation, where the targeted tissue has been damaged, but is not completely necrotic. As a result, although acute electrical isolation is achieved at the time of the procedure, conduction resumes across these gaps and at sites of prior ablation once the local tissue healing is complete.

Three-dimensional high-resolution navigator-echo myocardium delayed enhancement (3D-MDE) magnetic resonance imaging (MRI) has detailed the extent of scar from prior ablation in the left atrium (LA).[5–10] There are also reports of its use intra-procedurally[10–14] to improve success rates and minimize complications.[5,6] However, 3D-MDE requires gadolinium-Diethylenetriaminepentacetate (DTPA)

* Corresponding author. Tel: +1 617 643 4017; fax: +1 617 726 3852, E-mail: sdanik@partners.org

Published on behalf of the European Society of Cardiology. All rights reserved. © The Author 2013. For permissions please email: journals.permissions@oup.com.

Downloaded from https://academic.oup.com/europace/article/16/1/133/464598 by Akdeniz University user on 20 September 2021

What's new?

- This is the first translational work to describe the use of real-time assessment of circumferential lesions around the pulmonary veins using DENSE strain imaging.
- These data provide the basis for real-time magnetic resonance imaging of patients during pulmonary vein isolation to confirm that lesions are continuous without skipped areas of healthy, unablated tissue.

contrast administration, followed by a 20–30 min wait period. In addition, renal clearance forces extended intervals between repeated administrations. There is also concern that intra-procedural administration, during the course of progressive tissue ablation, may trap Gd-DTPA in non-perfused tissue for lengthy periods, possibly freeing toxic Gd ions.

It would be useful, therefore, to find a non-contrast alternative to 3D-MDE. T1-weighted imaging could provide a non-contrast alternative to 3D-MDE, but its sensitivity to tissue necrosis has a time delay and is not as strong.[11,15] Proton resonant frequency could potentially image the thermal dose directly, if its motion stability, susceptibility sensitivity, and spatial resolution are improved.[16,17]

Recent publications suggest that left ventricular (LV) scar from prior infarction can be detected by strain imaging, using MRI techniques such as tagging, HARP, SENC, or DENSE,[18–23] as well as intracardiac echo strain.[24–26] A recent seminal paper on ultrasound strain imaging of focused ultrasound ablation lesions,[27] has shown that abnormally high shear strains are created at the non-ablated immediate surroundings of ablation lesions. Along the same lines, data have suggested that both MRI and computed tomography can detect and quantify changes in contraction of the PVs in patients before and after PV isolation,[28–33] suggesting that wall-motion studies could differentiate non-elastic (ablated) wall from healthy (viable) wall.

We hypothesized that a high-resolution strain MRI sequence could detect displacement changes occurring in the PV ostia, and that, as in the LV, it would be possible to differentiate between rigid displacement, present in necrotic tissue, and elastic deformation, which signifies viable tissue.

This work details a high-resolution navigator-echo DENSE sequence that was developed for this purpose. Sequence testing in healthy animals was published previously.[34,35] The on-line supplement shows healthy sheep LV (*Figures 1* and *2*) and swine LA strain maps, as well as mean and standard deviations obtained for ventricular and atrial strain.[34,35]

After initial testing in an infarcted (LV) sheep, it was applied to LA imaging. To test atrial ablation gap detection, four swine models with incomplete circumferential ablation of the right superior pulmonary veins (RSPVs) were created and then imaged using 3D-MDE and DENSE.

Methods

The respiratory-navigator-echo electrocardiogram-gated DENSE sequence

Magnetic resonance imaging sequences can be sensitized to tissue strain, i.e. to changes in shape and volume. The key objectives are to measure displacements which occur as result of a force, as well as to remove those displacement that produce rigid-body motion, in which the entire tissue moves in unison, but in which there are no differential changes in volume or shape. The DENSE (Displacement Encoding with Stimulated Echoes) sequence, which uses displacement encoded stimulated echoes to encode motion in the MRI phase, was previously described[34–37] (*Figure 1C*). We utilized a 2D-DENSE sequence to measure strain in the two (x and y) in-plane directions. The displacement encoding (DE) preparation sub-sequence formed the first waveform of the sequence. It consisted of two 90° radiofrequency (RF) pulses with a magnetic-field gradient along a given direction (i.e. x or y) placed between them, and resulted in each pixel in the image being prescribed an initial phase shift, depending on its position along this spatial direction. The DE preparation strength (in mm/π-phase shift) depended on the gradient area that was used. After the DE waveform, a second sequence phase (a few hundred milliseconds) was provided, termed the mixing time (TM), in which the initial phase evolved due to the pixels being displaced along the selected magnetic-field gradient direction as a result of the physiological motion, which resulted in an additional phase increment, beyond the initial phase, being added. In the beginning of the third sequence phase, the initial phase of each pixel was removed, so that only the incremental phase of each pixel remained. In the last sequence phase, which is termed the readout phase, a multiple-echo fast spin echo (FSE) sequence of pulses was applied, which recorded the incremental phase shifts of each pixel.[36] The sequence was repeated several times to acquire first a reference phase map (a map in which a DE of zero was applied), and thereafter to encode for x and y displacements. Artifactual phase shifts resulting from free induction decay were removed with an inversion pulse during the mixing period,[36] and stimulated echo artefacts were removed by acquiring twice in each DE direction,[37] so that a complete implementation required six complete cycles of the sequence.

Detecting *cardiac* strain required that *respiratory* motion be small. A low-resolution $2.7 \times 2.7 \times 8\ mm^3$, 24 echo-train-length (ETL) FSE readout with two-directional encoding, such as used in the LV, requires 24 heart beats, approaching the maximal patient breath-holding time. In the thinner atrial wall, higher spatial resolution was required, with longer scan times needed to obtain the necessary signal-to-noise ratio (SNR so that a free-breathing acquisition needed to be performed. Recording the position of the anatomy at different portions of the respiratory cycle was accomplished by applying respiratory-navigator-echo pulses (*Figure 1A*) that tracked diaphragmatic motion. A 'pencil-beam' navigator echo[34,35] was repeated every 50 ms, exciting a 1 cm diameter cylindrical column at the right hemi-diaphragm, which detected superior–inferior respiratory motion of the diaphragm. These navigator echoes were repeated until the system detected that the diaphragm had returned to the desired (± 2 mm) end-expiration respiratory position. Once this condition was met, the system waited for the next cardiac R-wave and then acquired the DENSE pulse sequence (*Figure 1B*). Immediately after data acquisition, these navigator echoes were resumed. The system then compared the navigator echo which followed data acquisition with that of the navigator echo which immediately preceded acquisition, which served to indentify whether large respiratory motion had (>3 mm) occurred during the DENSE acquisition itself, which meant that respiratory motion, as opposed to cardiac motion, had been recorded. When above-threshold motion was exceeded, the data that had just been acquired were rejected and the data were later re-acquired. Utilizing this dual-navigator respiratory-triggered DENSE sequence, along with shorter imaging windows reducing motion during acquisition, higher resolution was achieved. Readout timing was set for the 'quiet' cardiac phases, LV end-systole (250–350 ms post-QRS), or at peak LA diastole (280–300 ms

Downloaded from https://academic.oup.com/europace/article/16/1/133/464598 by Akdeniz University user on 20 September 2021

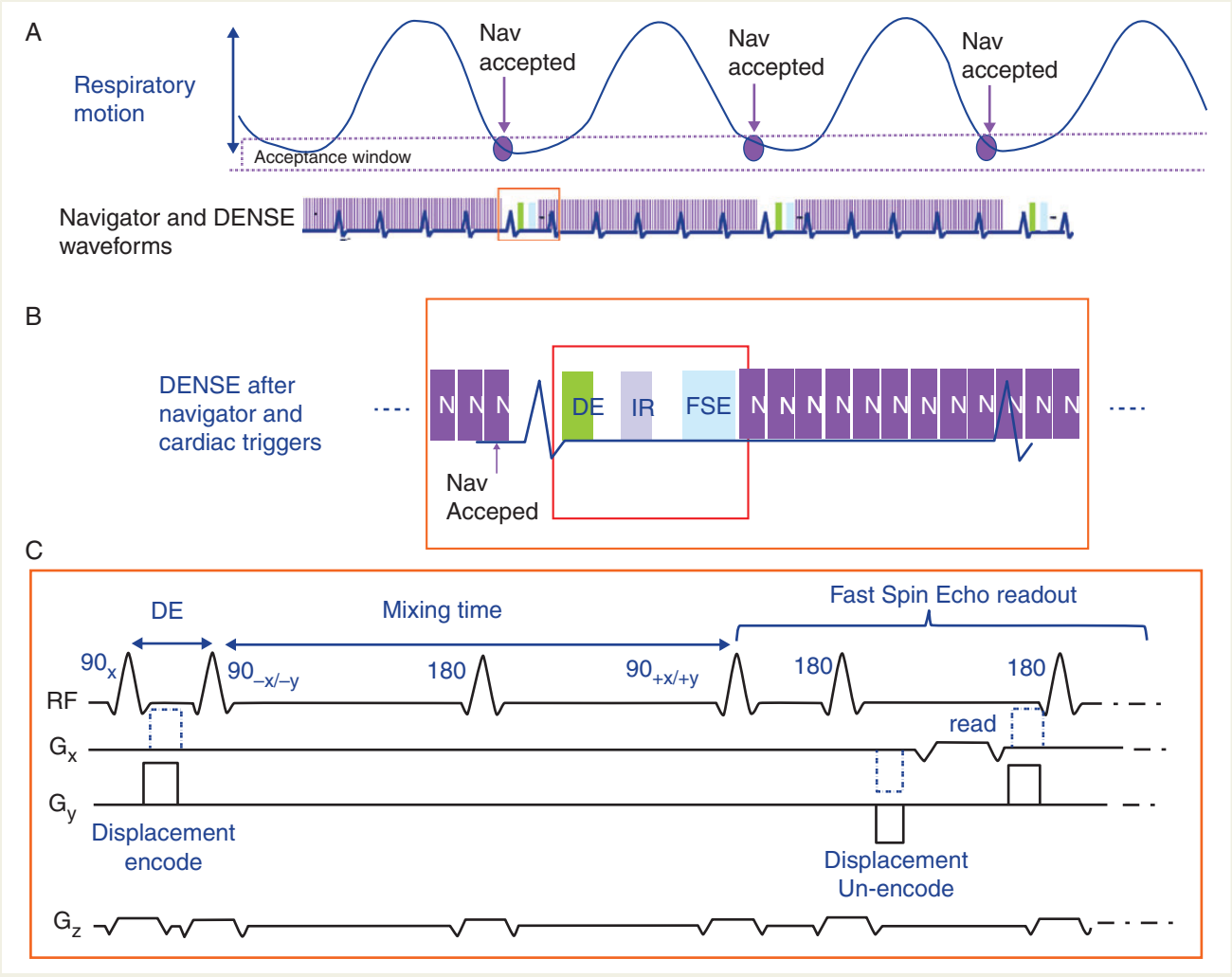


Figure 1 Respiratory-triggered META-DENSE sequence. (*A*) Diagram of respiratory cycle (upper), and waveform of cardiac-gated META-DENSE with surrounding respiratory navigator echoes (lower). Navigators are accepted when they fall in a pre-determined window in the respiratory cycle. (*B*) Enlarged view of one cardiac cycle, showing navigators preceding and following the META-DENSE sequence. When the navigator position criteria are met, the sequence waits for an ECG trigger, and then executed the DENSE pulse sequence. Navigators after DENSE are compared with those preceding the sequence, detecting the magnitude of motion occurring during image acquisition. If motion during acquisition is excessive, the data are rejected and re-acquired later on. (*C*) The META-DENSE pulse sequence, consisting of a DE (*D* and *E*) preparation, followed by a mixing time (TM) (~300 ms) in which displacement is measured. During the TM, an inversion pulse is played to suppress an anti-echo artefact. Finally, a multi-echo Fast Spin Echo readout (~140 ms) is played (only first echo is shown). META-DENSE is repeated three times; a reference scan without DE (no gradient between the two 90 s in the DE prep), followed by *x* encoding (dashed blue gradient) and *y* encoding (solid black). To further suppress artefacts, each *x* and *y* encode is repeated, with 90° RF phase modulation (from 90_{+x} to 90_{+y}) in the second repetition, which also increases the signal-to-noise.

post-QRS), as determined using MRI wall-motion 'cine' acquisitions in the ventricle and atrium.

Sequence parameters (LV, LA): resolution 1.0 × 1.0 × 4.0 (LV) or 1.2 × 1.0 × 4.0 mm^3 (LA), bandwidth ±64 kHz, ETL 16 (duration 100–140 ms), DE 5 mm/π (LV) or 4 mm/π (LA), TM 250–350 ms, two averages, and 5–7 min/slice.

Post-processing of DENSE data

Each DENSE acquisition produced three raw data files; containing the reference phase data (REF), along with the *x* displacement and the *y* displacement maps. Data processing to obtain strain maps were performed using IDL (ITT).[34,35] Magnitude and phase images were reconstructed from each raw data file. On the magnitude images, the internal and external borders of the desired region-of-interest (ROI) were manually drawn. The phase images, after being corrected for the reference phase and unwrapped, produced *x* and *y* displacement maps. The strain matrix, which represents the spatial derivatives of the *x* and *y* displacement along both *x* and *y*, was computed from the displacement maps within a 4 × 4 neighbourhood about each pixel, which resulted in a 2 × 2 strain matrix which retained the original spatial resolution. These matrices were diagonalized, providing two principle strain directions

Downloaded from https://academic.oup.com/europace/article/16/1/133/464598 by Akdeniz University user on 20 September 2021

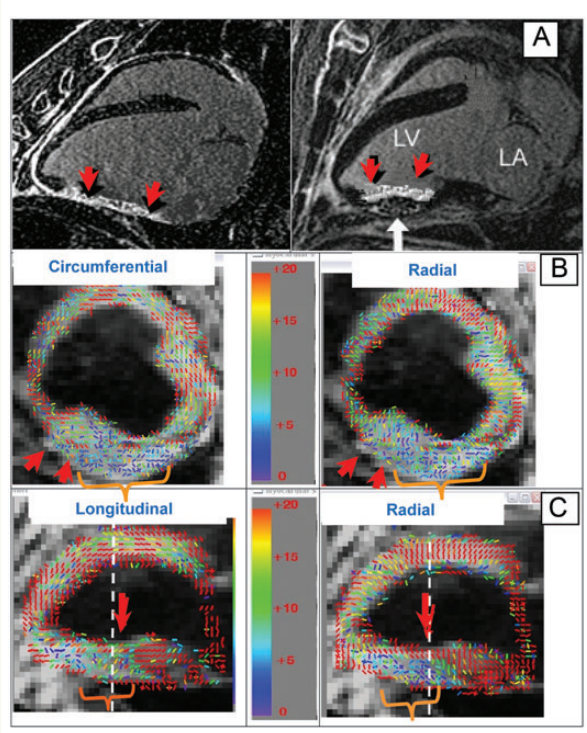


Figure 2 High-resolution respiratory-triggered DENSE of an infarcted sheep, with an inflated-balloon patch on the inferior wall of the LV to prevent remodelling (white arrow). (*A*) Two long-axis 3D-MDE images show mid-ventricular non-transmural scar (red arrow). (*B*) Colour-coded short-axis DENSE strain, showing strain-magnitudes ranging from normal (20%, red) to lack of strain (0%, blue). Circumferential strain (left) and radial strain (right). Chronic infarct and patch (orange bracket) appear as low-strain regions. (*C*) Long-axis DENSE strain, with longitudinal (left) and radial (right) strains. White dashed line indicates where short-axis images (*B*) intersect long-axis slice. Non-transmural infarct appears as large strain (live tissue) along the endocardial surface (right image) with low strain (necrosis) from the mid-wall to the epicardial surface. Note that the sign of radial strain is positive and circumferential strain is negative.

(eigenvectors) and amplitudes (eigenvalues). Match-sticks, denoting tissue-strain direction, were drawn at each pixel, with the strain magnitudes overlaid in colour. To improve the visualization, the cross-shaped match-sticks were separated into two groups, based on two differing criteria. In the LV alone, maps were produced according to the strain eigenvector direction; longitudinal strain, along the long axis's centre-line apex-to-base direction, radial strain, along the epicardial-to-endocardial direction, and circumferential strain, orientated perpendicular to the radial strain in a short-axis view. In the LA, they were separated by the eigenvalue polarity; positive (≥ 0) eigenvalues produced a myocardial-thickening map, and negative (<0) eigenvalues produced a myocardial-shortening map. Relative strain precision was estimated at 2%, based on repeated acquisitions of the same data in the LV. Processing time per image was <2 min on a standard laptop.

On the LA strain maps, regions of $<8\%$ strain were manually traced, highlighting regions suspected of being necrotic or stunned.

Animals and procedures

Four healthy 20–30 kg swine and two 30 kg sheep were used, under two animal-committee approved protocols. All animals were intubated in the animal laboratory, mechanically ventilated, and forcibly breath-held by shutting the ventilator. Other experimental details were previously described.[14,39] Heart rates ranged from 70–92 b.p.m.

Left-ventricular procedures

In two sheep, LV inferior-wall infarction was created in open surgery by ligating the second and third circumflex obtuse marginal branches.[38] An elastic patch was surgically placed around the animal's LV using open-heart surgery. An elongated oval balloon parallel to the LV long axis was contained between the patch and the myocardium, and sewn over the infarct region, so that balloon inflation displaced the myocardium inward.[39] Twelve weeks later, the animals were intubated and brought to the MRI suite.

Atrial procedures: electro-anatomic mapping and atrial ablation procedures

Mapping of the LA and RFA were performed in four swine. After pre-medication and general anaesthesia, introducer sheaths were placed in the femoral arteries and veins. Under fluoroscopic guidance (GE Healthcare OEC 9800), an 8.5 Fr Mullins sheath and a 0.035 inch guide-wire were advanced to the intra-atrial septum, followed by needle transseptal puncture. Once access to the LA was obtained, intravenous heparin (100 U/kg initial bolus, followed by 30 U/kg/h) was administered. The animals then underwent standard electro-anatomic (EAM) substrate mapping, using multispline penta-array mapping catheters and the CARTO XP system (Biosense-Webster).

With mapping complete, circumferential RFA of each swine's RSPV was performed using a 3.5 mm irrigated mapping/ablation catheter (Biosense Webster), with the ablation points marked on the EAM map. A gap in the ablation line was intentionally created in the circumferential line. One hour after RFA, the animals were transferred to the MRI lab. After imaging, the animals were sacrificed and the hearts stained for scar.

Magnetic resonance imaging procedure

Six MRI sequences were performed on a GE 1.5T scanner. Initially, electrocardiogram (ECG)-gated axial and sagittal fast gradient echo localizers were performed to localize the ventricular and atrial anatomy.

To obtain the timing of 'quiet', relatively motionless, cardiac phases, 12–14 prototype 2D Steady-State Free Precession[14,40] short-axis wall-motion slices were acquired, covering the LV or the LA.

Navigated 2D-DENSE imaging was then performed. In LV studies, eight slices were acquired, four along the LV short axis, covering the apex to base, and four radially, at 45° rotations, along the LV long axis. For the LA/PV studies, five slices were placed at the RSPV ostium, with four contiguous slices oriented perpendicular to the RSPV trunk's axis, and one along the trunk axis.

For high-resolution cardiac luminal anatomy visualization, 3D contrast-enhanced (0.44 cc/kg Gd-DTPA) ECG-gated MR angiography was performed, covering the entire heart as well as the aorta and inferior vena cava.[10,14]

To detect RFA lesions, 3D respiratory-navigated myocardium delayed enhancement (3D-MDE)[14] was performed 30 min after contrast injection; TR/TE/TI/θ = 3.5/0.9/150 ms/25°, $1.2 \times 1.2 \times 1.2$ mm^3 resolution, $\pm$62.5 kHz bandwidth, 4–6 min acquisition, timed to the LV end-systolic or the LA peak-diastolic 'quiet' phase.

Downloaded from https://academic.oup.com/europace/article/16/1/133/464598 by Akdeniz University user on 20 September 2021

Post-processing of three-dimensional magnetic resonance angiography and myocardial delayed enhancement data

The 3D-magnetic resonance angiography (MRA) data were segmented using the GE Advantage Windows (AW) to render the luminal surfaces of the LA and PVs.[14] The 3D-MDE data were then thresholded and manually segmented, leaving only regions bordering the atrial/PV lumen, and then overlaid on the luminal image using the AW's compare function, providing a volumetric display of vessel-wall scar superimposed on cardiac anatomy.

To compare 2D-DENSE slices with 3D-MDE, the MDE data were re-sliced into planes at the position, orientation, and slice-width of the DENSE data.

Statistical comparison of three-dimensional myocardial delayed enhancement and 2D-DENSE

For each swine, the cumulative total low-strain (<8%) area, on the five DENSE slices acquired perpendicular to the RPSV ostium, was measured and compared with the high MDE (>120% SNR) area observed in the reformatted MDE slices. An 8% strain was chosen as an indicator of low strain since it is one standard deviation (9%) below the mean of normal atrial tissue (18%).[34,35]

To measure 2D cross-correlation (Matlab 9B) the images were separately thresholded binarily; (i) MDE: 1, if pixel had signal intensity >150% of background, and 0 otherwise (ii) DENSE: 1 if pixel had <8% strain, and 0 otherwise. Two-dimensional normalized cross-correlation between MDE and DENSE was then performed on each of the five slices, and a five-slice mean computed.

Results

Left ventricular results

Left ventricular results were acquired for comparison with prior DENSE studies, which were primarily performed in the LV.

Figure 2 details results obtained from an infarcted sheep,[39] with an inflated-balloon patch on the inferior-wall restricting motion. *Figure 2A* shows two radial slices, reformatted from 3D-MDE, showing the infarct and the balloon patch (right image, white arrow). *Figure 2B* shows short-axis strain in the mid-ventricular wall. The inferior-wall patch creates a low strain and directionally disordered region, and the thin infarcted wall is also seen (red arrow). The long-axis strain (*Figure 2C*), clearly shows the non-transmural infarct (right image, red arrow), as well as the low strain on the inferior wall resulting from the balloon patch.

Left atrial results

Incomplete circumferential ablation around the RSPV was performed in all four animals, with correspondence between the ablation's 3D-MDE, strain, and histology signatures described.

Figure 3 summarizes findings from one swine. *Figure 3A1* and *A2* show EAM map projections, overlaid with the ablation points. The intentional ablation gap is marked (green arrow). *Figure 3B1* shows an LA and PV surface rendering, overlaid; *Figure 3B2* and *B3*, with a 3D-MDE scar rendering. Three-dimensional MDE (*Figure 3B3*) detected the gap in the ablation line surrounding the RSPV.

Figure 3B2 is overlaid with dotted white lines, denoting the location of the proximal and distal 2D-DENSE slices placed at the RSPV/LA ostium, perpendicular to the RSPV's axis.

Figure 3D1 and *D2* show strain results for the distal and proximal DENSE slices, respectively. White lines trace boundaries of small (<8%) and directionally disorganized strain, assumed to be ablated regions. Lack of circumferential RSPV ablation is apparent, with differing lesion sizes and positions in the distal and proximal slices. Large strains surround the ablated zones in the myocardial-shortening maps, corresponding to shear strains developed during atrial dilation. The ablated regions' area is smaller in the myocardial-shortening maps.

Figure 3E1 and *E2* are reformatted 3D-MDE slices at the DENSE-slice positions. The RSPV wall was traced on these images, since viable-wall geometry is hard to resolve on 3D-MDE images. It is clear that the wall is not circumferentially ablated, with most of the ablated wall lying in the superior (top) and right side of the images, with substantial gaps in the inferior and left walls. Comparing DENSE with MDE (*Figure 3D1* with *Figure 3E1*, and *Figure 3D2* with *Figure 3E2*), a correspondence appears between the areas of high strain and un-enhanced ablation gaps, whereas in the ablated regions, low and directionally disorganized strain is present. The correspondence between MDE and DENSE is strongest in the proximal slices.

Figure 3F is a stretched-out gross histology photograph of the LA wall in the region of the RSPV ostium. The stained transmural lesion regions were traced and the ablation gaps denoted. There is good correspondence between MDE, strain, and histology.

Figure 3G demonstrates findings in a second pig. *Figure 3G1* and *G2* show the EAM projections, overlaid with ablation point positions, with ablation gaps marked. In the luminal surfaces overlaid with the 3D-MDE (*Figure 3H2* and *H3*), it is apparent that the ablation line has large gaps, best seen in a cutout rendering (*Figure 3H3*).

Figure 3I1 and *I2* show the strain results for distal and proximal DENSE slices placed perpendicular to the RSPV's axis. There is low strain on the top portion of the veins, suggesting tissue necrosis, with high strains, indicating viable tissues, on the lower side. This is highly correlated with the MDE appearance (*Figure 3H3*).

To visualize strain in another orientation, a DENSE slice was acquired along the RSPV axis, with its position denoted in *Figure 3H4*. Since this slice covers two PVs, two ROIs were drawn, covering the ablated RSPV (*Figure 3J1*) and the adjacent right inferior pulmonary vein (RIPV, *Figure 3J2*), with strain results shown in *Figure 3K1* and *K2*, respectively. Since the PV walls are quite thin in this orientation, strain discrimination is more difficult, although the proximal right RSPV and the left RIPV walls have high strains, while the distal wall has low strain. A new finding from this image is that a large portion of the distal wall between the veins was ablated, which is consistent with the MDE results (*Figure 3H2*).

Figure 3L is a gross histology photo of the RSPV ostium region, overlaid with transmurally ablated regions. The ablation gaps are quite clear, shaped similarly to their strain-image appearance, *Figure 3I1* and *I2*.

The atrial statistical results are summarized in *Table 1*. The average low-strain DENSE areas measured 120 $\pm$ 30 vs. 90 $\pm$ 18 mm^2 for high 3D-MDE areas. The 2D geometric cross-correlation of ablated regions between 3D-MDE and 2D-DENSE is also shown,

Downloaded from https://academic.oup.com/europace/article/16/1/133/464598 by Akdeniz University user on 20 September 2021

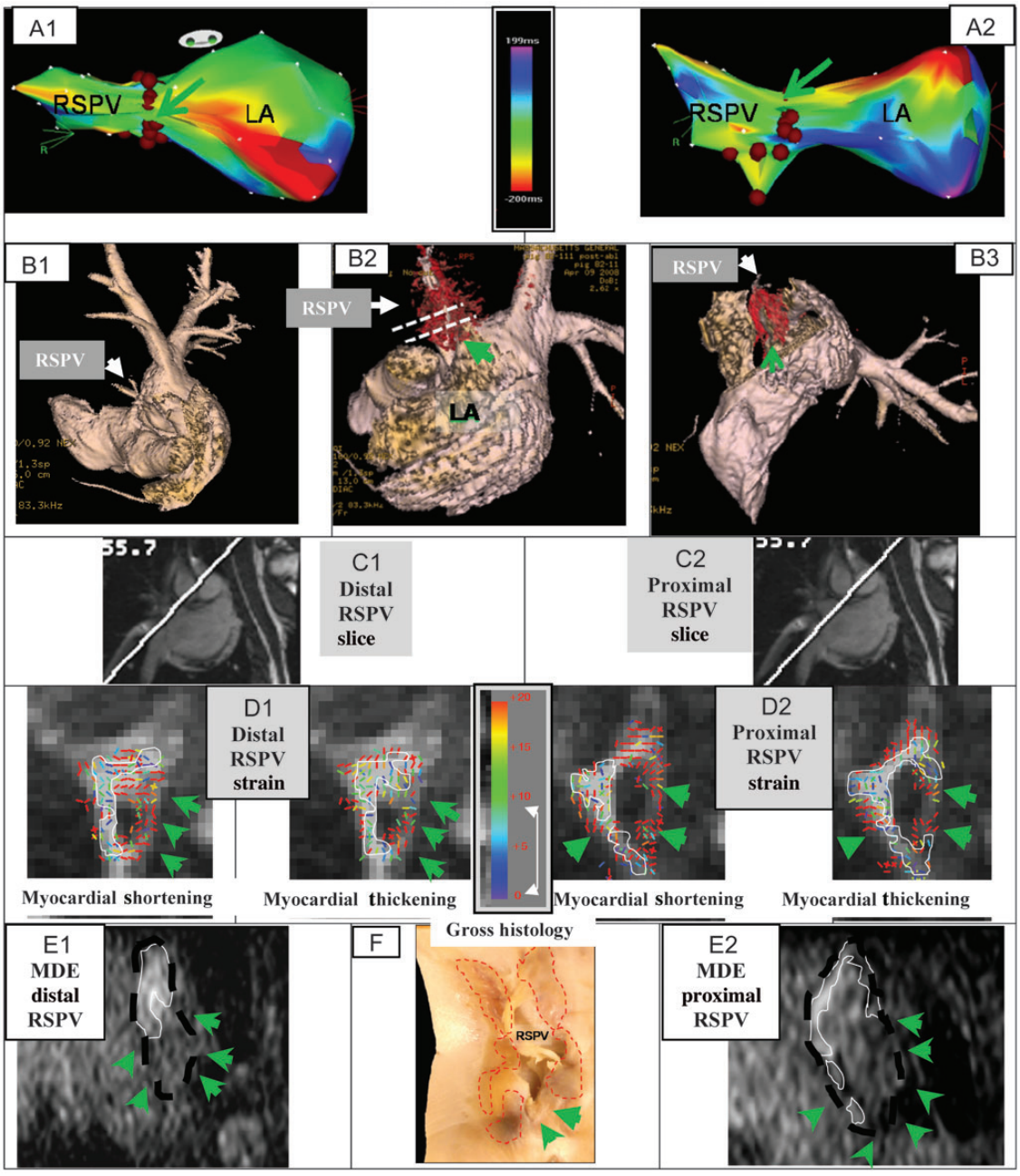


Figure 3 Incomplete RF ablation of two swine RSPV. The first swine includes figures *A*–*F*, the second swine includes figures *G*–*L*. (*A*) EAM maps overlaid with RFA points (brown dots); Anterior (*A1*) and Superior (*A2*) views, showing gaps (green arrows). Actual size of gaps could not be determined from EAM. Activation maps were obtained prior to ablation. (*B*) Atrial luminal renderings (pink), segmented from 3D-MRA, are overlaid with a 3D-MDE scar map (red), showing the gaps in RSPV ablation (*B2* and *B3*). (*C*) Images detailing the orientation of distal (*C1*) and proximal (*C2*) DENSE slices placed perpendicular to the RSPV ostium. Slice positions are also shown in 5B2. (*D*) Colour-coded DENSE myocardial shortening (negative sign) and myocardial-thickening (positive sign) strain magnitude for the distal (*D1*) and proximal (*D2*) slices. White lines outline regions with $<8\%$ strain. (*E*) Reformatted 3D-MDE slices at the position and orientation of *D1* (*E1*) and *D2* (*E2*). Dashed black line indicates position of RSPV wall, white lines outline enhanced ablated regions, and green arrows denote lack of enhancement (ablation gap). (*F*) Stained gross histology photograph of the LA wall at the RSPV ostium, overlaid with the areas (dashed red line) where transmural ablation lesions were found, with unstained ablation gaps denoted (green arrows). Incomplete RF ablation of the RSPV in another swine. (*G*) EAM maps overlaid with RFA points (brown dots); Anterior (*G1*) and Superior (*G2*) views, showing gaps (green arrows). Activation maps were obtained prior to ablation. (*H*) Luminal anatomy overlaid (*H1*–*H4*), with 3D-MDE scar, showing regions of incomplete ablation. Dashed white lines (*H2* and *H4*) designate positions of 2D-DENSE slices placed perpendicular and parallel to RSPV ostium. Colour-coded DENSE strain for the distal (*I1*) and proximal (*I2*) perpendicular slices. White lines outline, 8% strain regions. (*J*) Position of ROIs placed on DENSE slice oriented along the RSPV to RIPV plane (see *H4*); (*J1*) ROI (red) encompassing the RSPV, and (*J2*) ROI encompassing the RIPV. (*K*) Strain results for ROIs covering RSPV (*K1*) and RIPV (*K2*). (*L*) Gross histology photograph of the LA wall at the RSPV ostium region, overlaid with ablation lesion regions (dashed red line).

Downloaded from https://academic.oup.com/europace/article/16/1/133/464598 by Akdeniz University user on 20 September 2021

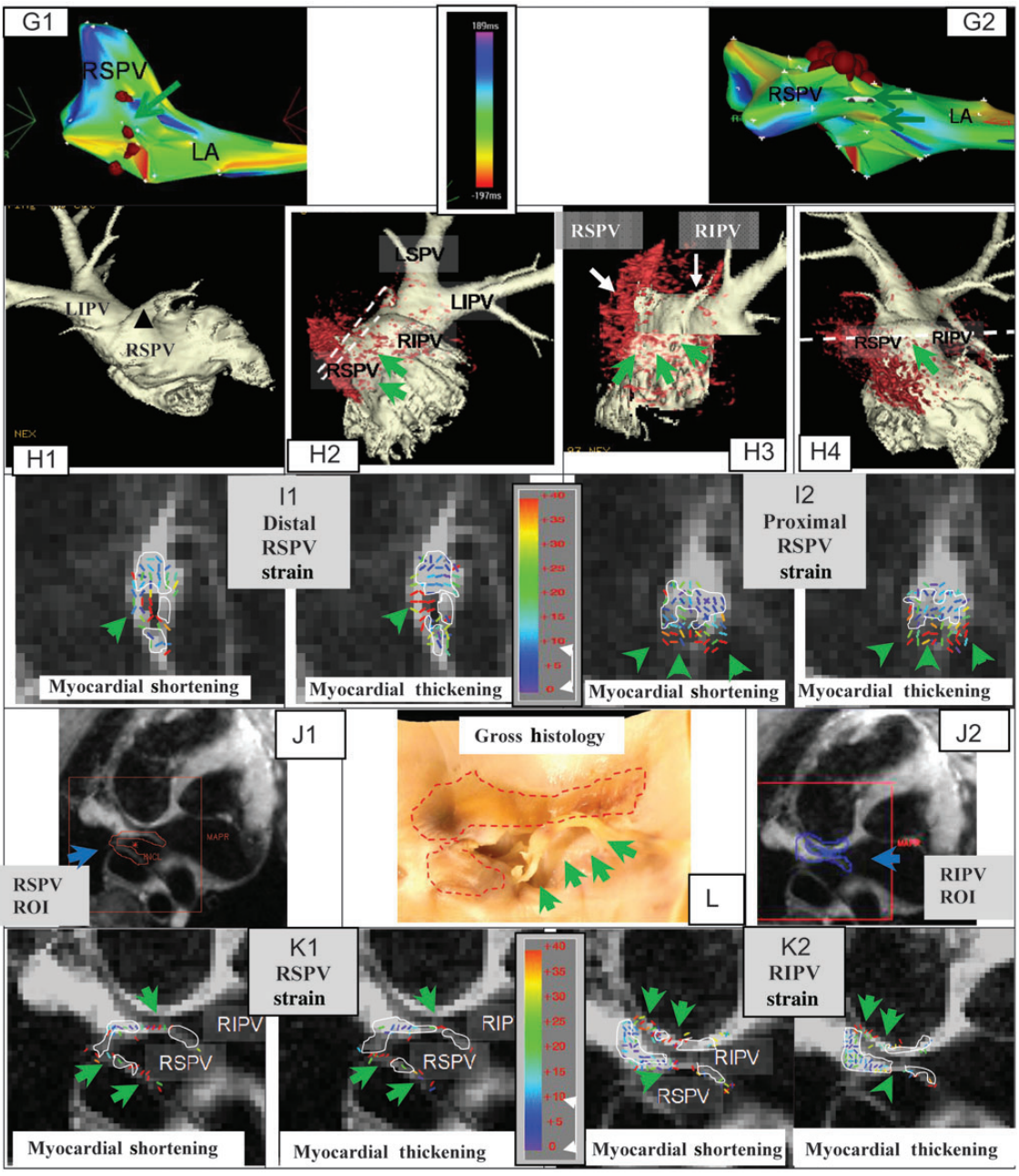


Figure 3 (continued).

with a four-swine average of 0.89 $\pm$ 0.05. These 2D correlations are statistically significant ($P < 0.05$), using a two-sided *t*-test.

Discussion

Millimeter in-plane-resolution strain images using navigator-echo-triggered 2D-DENSE were acquired in the LV and LA. By using navigator echoes, the DENSE acquisition time was extended beyond a single breath-hold, allowing for a shorter imaging window, and contributing to reduced respiratory contamination. By comparing navigator positions prior-to and after the imaging segment, motion during strain readout was further restricted, so that motional blurring was estimated at 0.3 $\times$ 0.3 mm^2. Signal averaging enabled the acquisition of higher spatial-resolution images at an acceptable image quality.

The LV results reproduced, at higher-resolution, DENSE results[18,19] obtained with breath-held DENSE, with strain accurately detailed infarcted as well as viable myocardium.

This high-resolution MRI LA strain study had 2–5 pixels spanning the PV wall. Imaging was performed at atrial diastole, where there is an extended 'quiet' phase, allowing maximal dilatation in the atria, so that small strain regions, combined with large adjacent shear stresses

Downloaded from https://academic.oup.com/europace/article/16/1/133/464598 by Akdeniz University user on 20 September 2021

Table 1 Statistical analysis of DENSE vs. MDE ablated region results for the four swine studied

Ablated swine (Figures where images shown)	DENSE area (mm^2)	MDE area (mm^2)	2D normalized cross-correlation
Pig #1 (*Figure 3*)	150	105	0.85
Pig #2	130	95	0.89
Pig #3 (*Figure 3*)	100	90	0.94
Pig #4	90	72	0.90

The five DENSE slices perpendicular to the PV ostium were compared with five reformatted MDE slices at the same slice positions and with the same slice thickness. Cross-correlation value is five-slice mean.

could confirm boundaries of ablated zones.[27] In LA DENSE, smaller DE gradients were utilized, relative to those used in the LV, reducing intra-voxel dephasing, and allowing for higher spatial resolution, but potentially reducing sensitivity to tissue necrosis.

Low-strain regions in the LA of the ablated swine were seen, which were highly correlated with ablated regions, as confirmed with both histology and 3D-MDE, suggesting that DENSE may be used as a non-contrast technique for detecting ablation lesions. The DENSE size of the ablated regions was somewhat larger than with 3D-MDE. This could be due to strain abnormalities extending beyond the ablated-tissue border, as seen in the LV.[23] This discrepancy could be reduced by using lower thresholds to characterize necrosis, or use of adjacent-tissue shear-strain amplification[27] to detect necrotic tissue.

While this work has shown that DENSE can detect gaps in the lesion set around the PV, it is important to highlight that it cannot yet acutely differentiate ablated tissue that is necrotic as compared with injured, oedematous tissue, which is a potential source of electrical reconnection. While it is likely that ablated tissue that is injured, but not yet necrotic, can be characterized by a surrounding spatial distribution of strain which appears different,[27] since such oedematous tissue is more compliant than necrotic tissue, further work is required to prove this hypothesis. While electrical isolation is achieved at the time of the index procedure, clinical recurrences occur due to conduction across healed tissue, whose most likely sources are reconnection in ablated areas that were injured, and not fully necrotic, as well as in gaps in the lesion set.

The data from this work have shown that DENSE is able to acutely detect tissue at the PV–LA junction that is still contractile, thus representing gaps in the lesion set. During the procedure, it is not uncommon for the vein to be electrically isolated before the circumferential lesion set is completed. Nevertheless, it is important to complete the lesion set to assure that isolation is permanent rather than transient, which is where DENSE can play a role.

Another important limitation of DENSE is that it can only be used when the heart is in sinus rhythm. While the hope is that imaging would be used at the end of PV isolation to look for gaps in the lesion set, it could only be performed in patients who are in sinus rhythm at the time of imaging. Patients who were cardioverted from longstanding AF during the procedure could not be reliably imaged due to the concern for atrial stunning, which would preclude the ability to detect contraction at the PV–LA junction. We did not include data examining the muscle sleeve spanning the LA and PV. Such data could have helped elucidate whether the gaps in the lesion sets included these sleeves, which could account for the findings from DENSE imaging.

Although human atria are ~50–100% larger in volume relative to swine, relaxing the spatial-resolution requirements, imaging of non-intubated humans, especially those with irregular cardiac rhythm, may require longer scan times, since navigator-echo-gated DENSE requires robust ECG-triggering, regular RR-intervals and fairly repeatable respiratory motion.

Two-dimensional DENSE currently utilizes only 20–30% of the RR-cycle for imaging. Replacing the physiological-cardiac motion with an externally driven atrial mechanical motion, potentially possible using ultrasonic or mechanical force[41,42] may increase strain's temporal efficiency and precision.

In conclusion, this study shows a high correlation between 2D-DENSE strain, 3D-MDE, and the histological signature of ablation lesions following RF ablation of PV ostia. DENSE may allow robust and repeated intra-procedural RF-ablation monitoring.

Acknowledgements

AHA SDG 10S0G2610139, NCRR/NCI 1U41RR019703-01A2, NIHLBI K23 HL68064.

Conflict of interest: The following authors have in the past or are currently employed by General Electric which manufactures imaging products: M.M.F., P.A.C., T.S., A.S., and S.N.G.

References

1. Fuster V, Rydén LE, Cannom DS, Crijns HJ, Curtis AB, Ellenbogen KA *et al.* ACC/AHA/ESC 2006 Guidelines for the Management of Patients with Atrial Fibrillation: a report of the American College of Cardiology/American Heart Association Task Force on Practice Guidelines and the European Society of Cardiology Committee for Practice Guidelines. *Circulation* 2006;**114**:e257–354.
2. Calkins H, Brugada J, Packer DL, Cappato R, Chen SA, Crijns HJ *et al.* HRS/EHRA/ECAS expert Consensus Statement on catheter and surgical ablation of atrial fibrillation: recommendations for personnel, policy, procedures and follow-up. A report of the Heart Rhythm Society (HRS) Task Force on catheter and surgical ablation of atrial fibrillation. *Heart Rhythm* 2007;**4**:816–61.
3. Cheema A, Dong J, Dalal D, Marine JE, Henrikson CA, Spragg D *et al.* Incidence and time course of early recovery of pulmonary vein conduction after catheter ablation of atrial fibrillation. *J Cardiovasc Electrophysiol* 2007;**18**:387–91.
4. Cheema A, Dong J, Dalal D, Vasamreddy CR, Marine JE, Henrikson CA *et al.* Long-term safety and efficacy of circumferential ablation with pulmonary vein isolation. *J Cardiovasc Electrophysiol* 2006;**17**:1080–5.
5. Badger TJ, Adjei-Poku YA, Burgon NS, Kalvaitis S, Shaaban A, Sommers DN *et al.* Initial experience of assessing esophageal tissue injury and recovery using delayed-enhancement MRI after atrial fibrillation ablation. *Circ Arrhythm Electrophysiol* 2009;**2**:620–5.
6. Dong J, Vasamreddy CR, Jayam V, Dalal D, Dickfeld T, Eldadah Z *et al.* Incidence and predictors of pulmonary vein stenosis following catheter ablation of atrial fibrillation using the anatomic pulmonary vein ablation approach: results from paired magnetic resonance imaging. *J Cardiovasc Electrophysiol* 2005;**16**:845–52.
7. Peters DC, Wylie JV, Hauser TH, Kissinger KV, Botnar RM, Essebag V *et al.* Detection of pulmonary vein and left atrial scar after catheter ablation with three-dimensional navigator-gated delayed enhancement MR imaging: initial experience. *Radiology* 2007;**243**:690–5.
8. Wylie JV, Peters DC, Essebag V, Manning WJ, Josephson ME, Hauser TH. Left atrial function and scar after catheter ablation of atrial fibrillation. *Heart Rhythm* 2008;**5**:656–62.
9. Verma A, Wazni OM, Marrouche NF, Martin DO, Kilicaslan F, Minor S *et al.* Pre-existent left atrial scarring in patients undergoing pulmonary vein antrum isolation: an independent predictor of procedural failure. *J Am Coll Cardiol* 2005;**45**:285–92.

Downloaded from https://academic.oup.com/europace/article/16/1/133/464598 by Akdeniz University user on 20 September 2021

10. Reddy VY, Schmidt EJ, Holmvang G, Fung M. Arrhythmia recurrence after atrial fibrillation ablation: can magnetic resonance imaging identify gaps in atrial ablation lines? *J Cardiovasc Electrophysiol* 2008;**19**:434–7.
11. Lardo AC, McVeigh ER, Jumrussirikul P, Berger RD, Calkins H, Lima J *et al.* Visualization and temporal/spatial characterization of cardiac radiofrequency ablation lesions using magnetic resonance imaging. *Circulation* 2000;**102**:698–705.
12. Dickfeld T, Kato R, Zviman M, Lai S, Meininger G, Lardo AC *et al.* Characterization of radiofrequency ablation lesions with gadolinium-enhanced cardiovascular magnetic resonance imaging. *J Am Coll Cardiol* 2006;**47**:370–8.
13. Dukkipati SR, Mallozzi R, Schmidt EJ, Holmvang G, d'Avila A, Guhde R *et al.* Electroanatomic mapping of the left ventricle in a porcine model of chronic myocardial infarction with magnetic resonance-based catheter tracking. *Circulation* 2008;**118**:853–62.
14. Schmidt EJ, Mallozzi RP, Thiagalingam A, Holmvang G, d'Avila A, Guhde R *et al.* Electro-anatomic mapping and radio-frequency ablation of porcine left atria and atrio-ventricular nodes using magnetic resonance catheter tracking. *Circ Arrhythm Electrophysiol* 2009;**2**:695–704.
15. Dickfeld T, Kato R, Zviman M, Nazarian S, Dong J, Ashikaga H *et al.* Characterization of acute and subacute radiofrequency ablation lesions with nonenhanced magnetic resonance imaging. *Heart Rhythm* 2007;**4**:208–14.
16. Grissom WA, Lustig M, Holbrook AB, Rieke V, Pauly JM, Butts-Pauly K. Reweighted l1 referenceless PRF shift thermometry. *Magn Reson Med* 2010;**64**:1068–77.
17. Kolandaivelu A, Zviman MM, Castro V, Lardo AC, Berger RD, Halperin HR. Noninvasive assessment of tissue heating during cardiac radiofrequency ablation using MRI thermography. *Circ Arrhythm Electrophysiol* 2010;**3**:521–9.
18. Aletras AH, Tilak GS, Natanzon A, Hsu LY, Gonzalez FM, Hoyt RF Jr *et al.* Retrospective determination of the area at risk for reperfused acute myocardial infarction with T2-weighted cardiac magnetic resonance imaging: histopathological and Displacement Encoding with Stimulated Echoes (DENSE) functional validations. *Circulation* 2006;**113**:1865–70.
19. Ashikaga H, Mickelsen SR, Ennis DB, Rodriguez I, Kellman P, Wen H *et al.* Electromechanical analysis of infarct border zone in chronic myocardial infarction. *Am J Physiol Heart Circ Physiol* 2005;**289**:H1099–105.
20. Ibrahim eH, Stuber M, Fahmy AS, Abd-Elmoniem KZ, Sasano T, Abraham MR *et al.* Real-time MR imaging of myocardial regional function using strain-encoding (SENC) with tissue through-plane motion tracking. *J Magn Reson Imaging* 2007;**26**:1461–70.
21. Korosoglou G, Youssef AA, Bilchick KC, Ibrahim el-S, Lardo AC, Lai S *et al.* Real-time fast strain-encoded magnetic resonance imaging to evaluate regional myocardial function at 3.0 Tesla: comparison to conventional tagging. *J Magn Reson Imaging* 2008;**27**:1012–8.
22. Agarwal HK, Prince JL, Abd-Elmoniem KZ. Total Removal of Unwanted Harmonic Peaks (TruHARP) MRI for single breath-hold high-resolution myocardial motion and strain quantification. *Magn Reson Med* 2010;**64**:574–85.
23. Garot J, Lima JA, Gerber BL, Sampath S, Wu KC, Bluemke DA *et al.* Spatially resolved imaging of myocardial function with strain-encoded MR: comparison with delayed contrast-enhanced MR imaging after myocardial infarction. *Radiology* 2004;**233**:596–602.
24. Hijazi ZM, Shivkumar K, Sahn DJ. Intracardiac echocardiography during interventional and electrophysiological cardiac catheterization. *Circulation* 2009;**119**:587–96.
25. Bunch TJ, Weiss JP, Crandall BG, Day JD, DiMarco JP, Ferguson JD *et al.* Image integration using intracardiac ultrasound and 3D reconstruction for scar mapping and ablation of ventricular tachycardia. *J Cardiovasc Electrophysiol* 2010;**21**:678–84.
26. Peichl P, Kautzner J, Gebauer R. Ablation of atrial tachycardias after correction of complex congenital heart diseases: utility of intracardiac echocardiography. *Europace* 2009;**11**:48–53.
27. Thittai AK, Galaz B, Ophir J. Visualization of HIFU-induced lesion boundaries by axial-shear strain elastography: a feasibility study. *Ultrasound Med Biol* 2011;**37**:426–33.
28. Kuppahally SS, Akoum N, Burgon NS, Badger TJ, Kholmovski EG, Vijayakumar S *et al.* Left atrial strain and strain rate in patients with paroxysmal and persistent atrial fibrillation: relationship to left atrial structural remodeling detected by delayed-enhancement MRI. *Circ Cardiovasc Imaging* 2010;**3**:231–9.
29. Thiagalingam A, Reddy VY, Cury RC, Abbara S, Holmvang G, Thangaroopan M *et al.* Pulmonary vein contraction: characterization of dynamic changes in pulmonary vein morphology using multiphase multislice computed tomography scanning. *Heart Rhythm* 2008;**5**:1645–50.
30. Atwater BD, Wallace TW, Kim HW, Hranitzky PM, Bhanson TD, Hegland DD *et al.* Pulmonary vein contraction before and after radiofrequency ablation for atrial fibrillation. *J Cardiovasc Electrophysiol* 2011;**22**:169–74.
31. Bowman AW, Kovacs SJ. Prediction and assessment of the time-varying effective pulmonary vein area via cardiac MRI and Doppler echocardiography. *Am J Physiol Heart Circ Physiol* 2005;**288**:H280–6.
32. Patel AR, Fatemi O, Norton PT, West JJ, Helms AS, Kramer CM *et al.* Cardiac cycle-dependent left atrial dynamics: implications for catheter ablation of atrial fibrillation. *Heart Rhythm* 2008;**5**:787–93.
33. Miquel ME, Hill DL, Baker EJ, Qureshi SA, Simon RD, Keevil SF *et al.* Three- and four-dimensional reconstruction of intra-cardiac anatomy from two-dimensional magnetic resonance images. *Int J Cardiovasc Imaging* 2003;**19**:239–54; discussion 255–256.
34. Fung MM, Aksit P, Gupta SN, Shankaranarayanan A, Beatty PJ, Aletras AH *et al.* Respiratory triggered DENSE imaging with navigator echoes: initial experience.In *Proceedings of the International Society for Magnetic Resonance in Medicine*. paper 701, Toronto, ON, 2008.
35. Aksit P, Shankaranarayanan A, Gupta SN, Beatty PJ, Aletras AH, Fung MM *et al.* Externally calibrated K-space based parallel reconstruction for DENSE imaging: initial experience. In *Proceedings of the International Society for Magnetic Resonance in Medicine*. paper 700, Toronto, ON, 2008.
36. Aletras AH, Ding S, Balaban RS, Wen H. DENSE: displacement encoding with stimulated echoes in cardiac functional MRI. *J Magn Reson* 1999;**137**:247–52.
37. Aletras AH, Arai AE. Meta-DENSE complex acquisition for reduced intravoxel dephasing. *J Magn Reson* 2004;**169**:246–9.
38. Goldfarb JW, Shinnar M. Free-breathing delayed hyperenhanced imaging of the myocardium: a clinical application of real-time navigator echo imaging. *J Magn Reson Imaging* 2006;**24**:66–71.
39. Chaput M, Handschumacher MD, Guerrero JL, Holmvang G, Dal-Bianco JP, Sullivan S *et al.* Mitral leaflet adaptation to ventricular remodeling: prospective changes in a model of ischemic mitral regurgitation. *Circulation* 2009;**120**:S99–103.
40. Slavin GS, Rettmann DW. Addressing efficiency and residual magnetization cross talk in multi-slice 2D steady-state free precession imaging of the heart. *Magn Reson Med* 2005;**53**:965–9.
41. Fahey BJ, Nightingale KR, McAleavey SA, Palmeri ML, Wolf PD, Trahey GE. Acoustic radiation force impulse imaging of myocardial radiofrequency ablation: initial in vivo results. *IEEE Trans Ultrason Ferroelectr Freq Control* 2005;**52**:631–41.
42. McDannold N, Maier SE. Magnetic resonance acoustic radiation force imaging. *Med Phys* 2008;**35**:3748–58.

Downloaded from https://academic.oup.com/europace/article/16/1/133/464598 by Akdeniz University user on 20 September 2021